

Cite this: DOI: 00.0000/xxxxxxxxxx

## Electronic Supplementary Information - How heat controls fracture: the thermodynamics of creeping and avalanching cracks

Tom Vincent-Dospital,<sup>a,b</sup> Renaud Toussaint,<sup>a,b</sup> Stéphane Santucci,<sup>c,d</sup> Loïc Vanel,<sup>e</sup> Daniel Bonamy,<sup>f</sup> Lamine Hattali,<sup>g</sup> Alain Cochard,<sup>a</sup> Eirik G. Flekkøy,<sup>b</sup> and Knut Jørgen Måløy<sup>b</sup>

Received Date

Accepted Date

DOI: 00.0000/xxxxxxxxxx

This document is an Electronic Supplementary Information. References to the related main manuscript<sup>†</sup> are marked with an M. For instance, a reference to the first equation in this main manuscript will be written as Eq. (M1).

### 1 Method for the measure of crack velocity versus energy release rate in PMMA

As part of the PMMA data was not published before (i.e., the slow propagation branch), we describe, in this section, the method that was used to acquire it.

Wedge splitting fracture tests are used to measure both the slow and fast  $V(G)$  branches in PMMA<sup>1,2</sup>, whose geometry is shown in Fig. 1. Rectangular plates of size 140 mm × 125 mm × 15 mm are first machined from a plate of moulded PMMA (Perspex<sup>®</sup>). A 25 mm × 25 mm notch is subsequently cut out on one of the two lateral edges and a 8-mm-long 800- $\mu$ m-thick groove is finally introduced in the middle of the notch with a diamond saw.

To grow slow cracks, an additional seed crack ( $\sim 2$  mm-long) is added at the end of the groove via a razor blade. This crack is loaded in tension by pushing a steel wedge (semi-angle of 15°) in the notch. Two steel blocks equipped with rollers are placed in between the wedge and the specimen notch to limit the parasitic mechanical dissipation through plastic deformations or friction at loading contacts. As a result, the vicinity of the crack tip can be assumed to be the sole dissipation source for mechanical energy

in the system. The wedge speed is first set to 1.6  $\mu$ m s<sup>-1</sup>. The force  $F$ , applied by the wedge to the specimen, increases linearly with time up to a point  $F_c$  above which the seed crack starts to propagate. Above this point,  $F$  decreases with time. We let the crack propagate over a distance of about 10 mm. This ensures reproducible initial conditions with a long-enough well-defined sharp seed crack. The specimen is then unloaded (unloading wedge speed: 16  $\mu$ m s<sup>-1</sup>). The specimen is then loaded again at a constant prescribed wedge speed  $V_{\text{wedge}}$ , which has been varied from 1.6  $\mu$ m s<sup>-1</sup> to 1.2 mm s<sup>-1</sup>.

During each fracture test, the force  $F(t)$  is monitored in real-time via a cell force mounted on the system (S-type Vishay load cell). A camera (USB2 uEye from IDS) is also used to image crack propagation at the specimen surface (space and time accuracy of 125  $\mu$ m and 0.1 s). A coarse approximation of the crack speed can be obtained by differentiating the position of the crack tip observed on the successive images. However, a more accurate signal  $V(t)$  is obtained from the force signal (see Ref.<sup>3</sup> for details on the method). Indeed, in a linear elastic isotropic material like PMMA, the specimen stiffness  $k(t) = F(t)/(V_{\text{wedge}}t)$  is a continuous decreasing function of the crack length,  $c(t)$ , that is set by the specimen geometry only. This function has been obtained using finite element calculations on the exact experimental geometry (Cast3M software, 2D simulation assuming plane stress conditions); it was checked that the obtained  $k$  versus  $c$  curve coincides with the experimental curves obtained by plotting  $k(t)$  as a function of the crack length measured by the camera. The idea is then to use this curve  $k(c)$ , and the corresponding inverse function  $k^{-1}$ , to infer the time evolution of crack length  $c(t)$  from the signal  $F(t)$ :  $c(t) = k^{-1}[F(t)/(V_{\text{wedge}}t)]$ . Time derivation of the so-obtained  $c(t)$  provides a signal  $V(t)$  about 50 times less noisy than that directly obtained from the camera images. The knowledge of  $c(t)$  and  $F(t)$  also allows determining the time evolution of the energy release rate,  $G(t)$ . Indeed, the total amount of mechanical energy provided to the specimen is  $F^2(t)/[2k(c(t))]$ . Differenti-

<sup>a</sup> Université de Strasbourg, CNRS, Institut de Physique du Globe de Strasbourg, UMR 7516, F-67000 Strasbourg, France; E-mail: vincentdospital@unistra.fr, renaud.toussaint@unistra.fr.

<sup>b</sup> SFF Porelab, The Njord Centre, Department of physics, University of Oslo, N-0316 Oslo, Norway.

<sup>c</sup> Université de Lyon, ENS de Lyon, Université Claude Bernard, CNRS, Laboratoire de Physique, F-69342 Lyon, France.

<sup>d</sup> Mechanics of disordered media laboratory, Lavrentyev Institute of Hydrodynamics of the Russian Academy of Science.

<sup>e</sup> Université de Lyon, Université Claude Bernard, CNRS, Institut Lumière Matière, F-69622 Villeurbanne, France.

<sup>f</sup> Université Paris-Saclay, CNRS, CEA Saclay, Service de Physique de l'Etat Condensé, F-91191 Gif-sur-Yvette, France.

<sup>g</sup> Université Paris-Saclay, Univiversité Paris-Sud, FAST, CNRS, Orsay, France.

<sup>†</sup>The main manuscript related to this Electronic Supplementary Information (ESI) is available at: ...

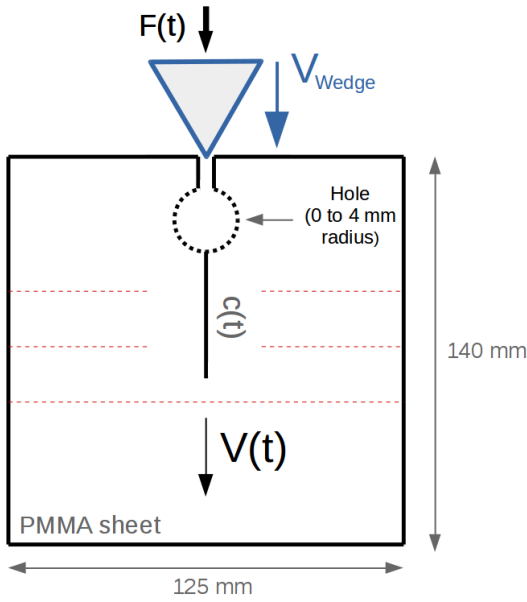


Fig. 1 Schematic of the experimental set-up used to measure the crack energy release rate  $G$  and its corresponding propagation velocity  $V(t)$  in PMMA. See Refs. <sup>1,2</sup> for details. The hole is used to store some potential energy in the PMMA sheet for fast propagation experiments and is replaced by only a seed crack for slow ones. The dashed horizontal lines represent conductive metallic lines deposited onto the sample to measure the fast crack velocity with an oscilloscope.

ating this stored energy with respect to  $c$  directly provides  $G(t)$ . The slow branch of Fig. M3 then provides the observed  $V(t)$  as a function of  $G(t)$ . The results from twelve fracture experiments are gathered in this branch and differ by their  $V_{\text{wedge}}$  value. To grow fast cracks and measure  $V(G)$  in the fast stable phase, the seed crack has been replaced by a hole of tunable radius (1 to 4 mm) drilled at the end of the groove<sup>1</sup>. This delays fracture and increases the potential energy stored in the specimen at the initiation of crack growth. The time evolution of  $V(t)$  is measured by monitoring, via an oscilloscope, the successive rupture of parallel 500- $\mu\text{m}$ -large metallic lines (chromium/gold) deposited on the surface. That of the stress intensity factor  $K$  is obtained via finite element analysis (see Ref. <sup>1</sup> for details). The time evolution of the mechanical energy release rate is then deduced:  $G = K^2/E$  where the Young modulus  $E$  in the studied PMMA have been measured to be  $E = 2.8 \text{ GPa}$ . The fast branch of Fig. M3 then provides the observed  $V(t)$  as a function of  $G(t)$ . The results from five fracture experiments are gathered in this branch; they differ by the amount of stored elastic energy at crack growth initiation.

## 2 Parameters sensitivity

We here show, on the PMMA data, how varying the model parameters around their inferred values impacts the model fit, thus giving the reader a better feeling for their individual effect and sensitivity. In each of the figures 2 to 8, a unique parameter of the model varies while the others are kept to the exact values used for the fit presented in Fig. M3:  $\xi = 56 \text{ nm}$ ,  $V_0 = 880 \text{ m s}^{-1}$ ,  $G_c = 1275 \text{ J m}^{-2}$ ,  $G_h = 650 \text{ J m}^{-2}$ ,  $\phi = 20\%$ ,  $\lambda = 0.18 \text{ J s}^{-1} \text{ m}^{-1} \text{ K}^{-1}$ ,  $C = 1.5 \times 10^6 \text{ J m}^{-3} \text{ K}^{-1}$ ,  $l = 1 \text{ nm}$  and  $T_0 = 296 \text{ K}$ . These seven plots

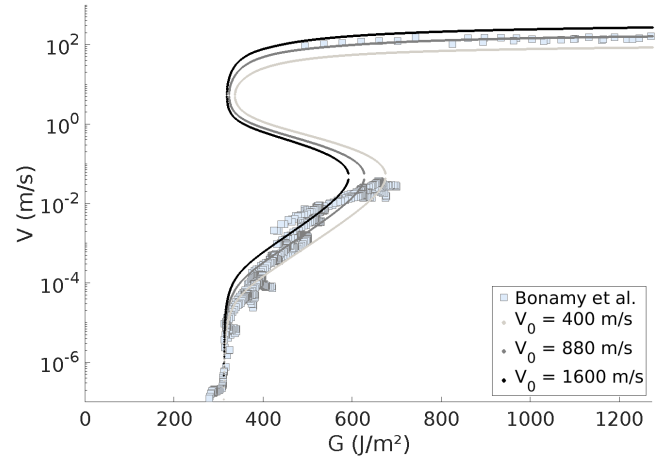


Fig. 2 Effect of varying the nominal velocity,  $V_0$ , on the fit to the PMMA data. The propagation velocity is roughly proportional to  $V_0$ , but also modifies the positions of the phase transitions.

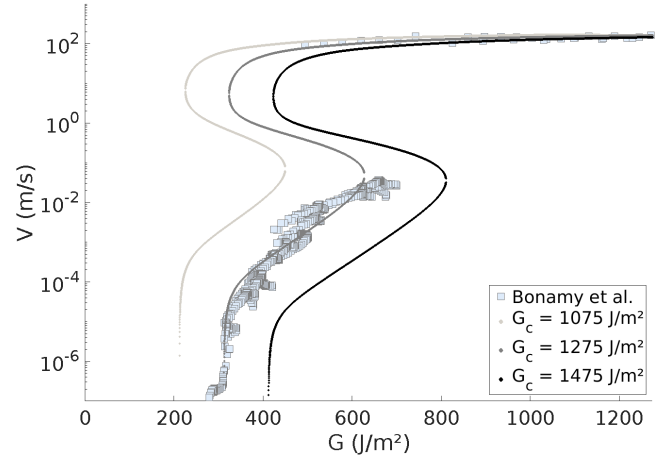


Fig. 3 Effect of varying the breaking energy barrier,  $G_c$ , on the fit to the PMMA data. At a given load  $G$ , the higher  $G_c$ , the slower the crack. The transitions between the three propagation modes (fast, slow, and dominated by healing) are also affected: a medium with a stronger barrier needs a heavier load to transit to a weaker state.

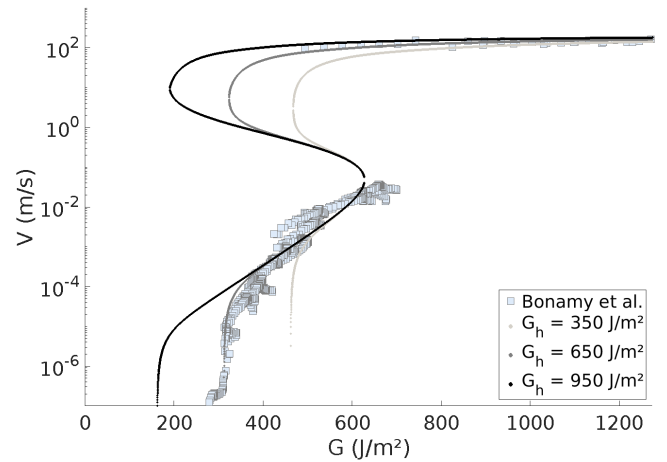


Fig. 4 Effect of varying the healing energy barrier,  $G_h$ , on the fit to the PMMA data. A crack that heals more easily needs a higher load to actually propagate forward or to stay in the high velocity regime.

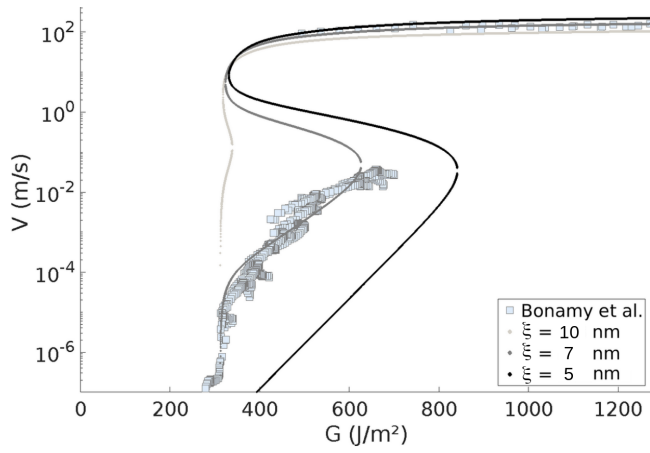


Fig. 5 Effect of varying the stress cut-off scale  $\xi$ , on the fit to the PMMA data.  $\xi$  mainly controls the slope and the intercept of the low velocity branch. A small change in  $\xi$  significantly modifies this branch as well as the threshold to the fast regime.

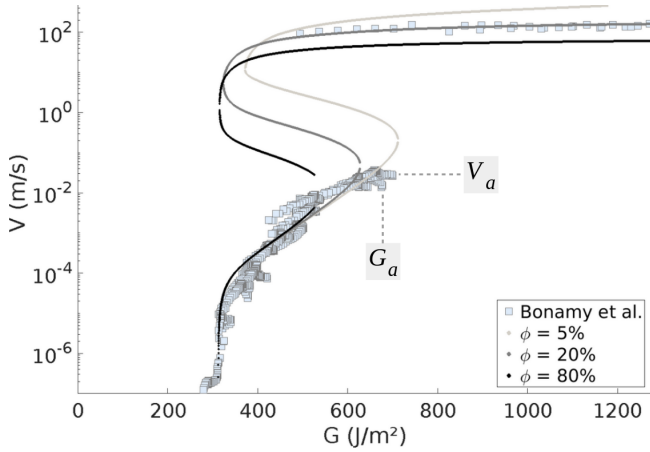


Fig. 6 Effect of varying the ratio of energy converted to heat,  $\phi$ , on the fit to the PMMA data. The maximum velocity increases with  $\phi$  as the tip temperature is higher. The threshold from the slow to the fast branch (i.e., the  $(G_a, V_a)$  point) shifts towards a lower  $G$  as a lighter load is required for the temperature to significantly deviate from  $T_0$ .

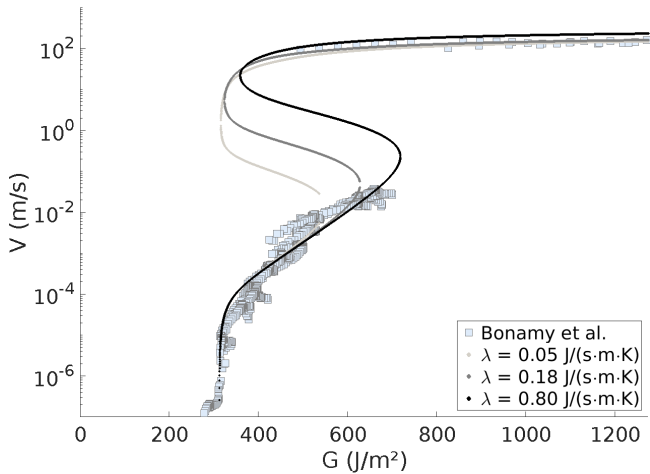


Fig. 7 Effect of varying the thermal conductivity,  $\lambda$ , on the fit to the PMMA data. With a higher  $\lambda$ , the heat is better evacuated: the slow to fast branch threshold shifts towards higher  $G$  and  $V$ . The fast regime is not very sensitive to  $\lambda$ , as  $\Delta T$  is there constrained by  $l$ .

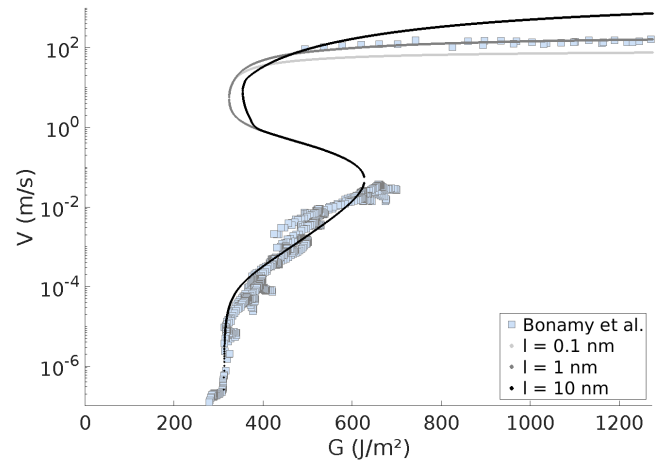


Fig. 8 Effect of varying the heat production zone radius,  $l$ , on the fit to the PMMA data.  $l$  mainly impacts the plot curvature on the high velocity branch. No effect is observed on the slow branch, as the thermal elevation there is constrained by the diffusion skin depth rather than by  $l$  (see Eq. (M6)).

show the fits up to the apparition of the secondary micro-cracks (see section M3.2 and Fig. M4), after which the model does not apply as such.

Naturally, some care should be taken when interpreting the inverted parameters (i.e.,  $\xi$ ,  $G_c$ ,  $G_h$ ,  $\phi$  and  $l$ ) beyond their actual orders of magnitude. For instance,  $\xi$  and  $G_c$  were fitted by a linear regression (i.e., Eq. (M8)) on the data which lies between  $G = 350$  and  $G = 700 \text{ J m}^{-2}$  in Fig. M3, and the above values ( $\xi = 56 \text{ nm}$  and  $G_c = 1275 \text{ J m}^{-2}$ ) were obtained with a coefficient of determination  $R^2$  equal to 0.85. Allowing  $R^2$  to drop down to 0.75 during this fit gives  $\xi$  in a 30 to 80 nm range and  $G_c$  between 950 and  $1500 \text{ J m}^{-2}$ .  $G_h$  being directly deduced from  $G_c$  (and from the vertical asymptote at low velocity in Fig. M3), the uncertainty on its value is comparable to that of  $G_c$ , that is, a few hundreds of joules per square meter. Let us now assess the accuracy of  $\phi$ . In the model, this parameters mainly controls which is the fastest point of the slow velocity branch (e.g., as shown in Fig. 6), after which cracks have to avalanche<sup>4</sup>. We then compare the experimental value for this particular point (obtained at  $G = G_a$  and  $V = V_a$ , see Fig 6) to the model prediction of the same point. We quantify the error there as the euclidean distance between these points, in the sense of Eq. (M9). Such a relative, unitless, error minimizes to 10% for  $\phi = 0.25$  and, should we allow it to rise up to 30%, we obtain  $\phi$  to be between 0.15 and 0.30. Finally, let us assess the accuracy of the inversion for the length scale of the heat production zone  $l$ . We vary  $l$  and compute the same relative euclidean error in average over the fast velocity branch (i.e., the location where the model is mostly sensitive to  $l$ , see Fig. 8). This error now minimizes to 5% for  $l = 1 \text{ nm}$  and, letting it reach 30%, we infer  $l$  to lie in a 0.1 nm to 2 nm range.

These uncertainties in the parameter inversion are somewhat high, but we here quantify an atomic scale process based on macroscopic measurements, so that this is not particularly surprising. One also needs to add up the experimental inaccuracy for  $V$  and  $G$  (see the data spread in Fig. M3), as well as the lim-

itations of our very first order physical model, as discussed in section M4.2. Still, overall, the data is well explained over eight decades of velocities and with parameters that are in physically reasonable orders of magnitude.

### 3 Data binning to compute a mean fit error

To compute a mean fit error  $\bar{\epsilon} = \text{mean}_d(\epsilon_d)$ , where  $\epsilon_d$  is defined by Eq. (M9), we first binned the PMMA and PSA data points onto coarse bins using a running average on both stable branches, as explained in the core text<sup>†</sup>. This was done to avoid the densely populated parts of the data sets to dominate on the value of the inferred  $\bar{\epsilon}$ . Figures 9 and 10 show the result of this data decimation.

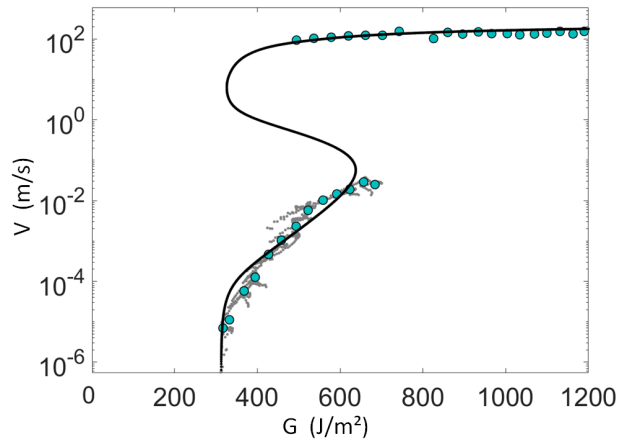


Fig. 9 Under sampled PMMA data (blue circles), using a running average on  $40 \text{ J m}^{-2}$  bins. The dots are the original data points and the black line the fitted model. With this decimated data set, the mean fitting error is  $\bar{\epsilon} = 4\%$ . The data is only shown to the onset of micro-cracking, beyond which the model does not apply as such.

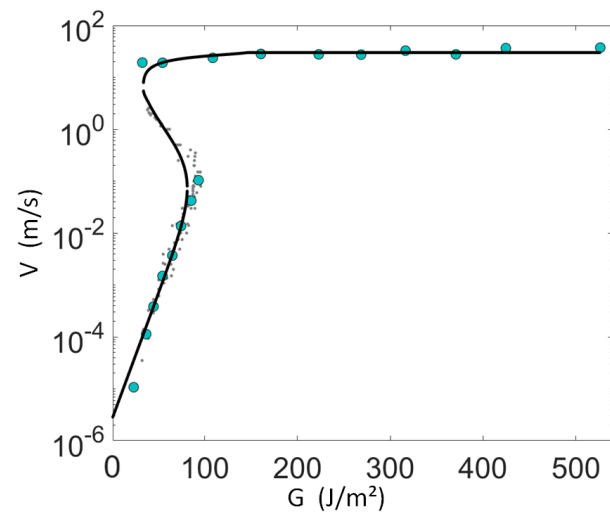


Fig. 10 Under sampled PSA data (blue circles), using a running average on  $10 \text{ J m}^{-2}$  bins. The dots are the original data points and the black line the fitted model. With this decimated data set, the mean fitting error is  $\bar{\epsilon} = 5\%$ .

## 4 Healing processes in tape

We considered the healing processes to be negligible in order to describe the dynamics of unrolling tape, as no low velocity constant  $G$  asymptote arising from crack healing displays in the  $(G, V)$  data (i.e., in Fig. M4). Such an absence would, however, also happen if  $G_c$  was to be smaller than  $G_h$ , as the asymptote is obtained for  $(G_c - C_h)/2$ . Thus, the healing energy barrier could still be comparable to the breaking one, and so still significantly impact the high velocity propagation branch, when the crack tip is hot enough for healing to be non negligible (as predicted by Eq. (M4)). Of course, an accurate quantification of this effect suffers from the absence of the asymptote as it is the only good constraint for  $G_h$ . Figure 11 shows for instance a model

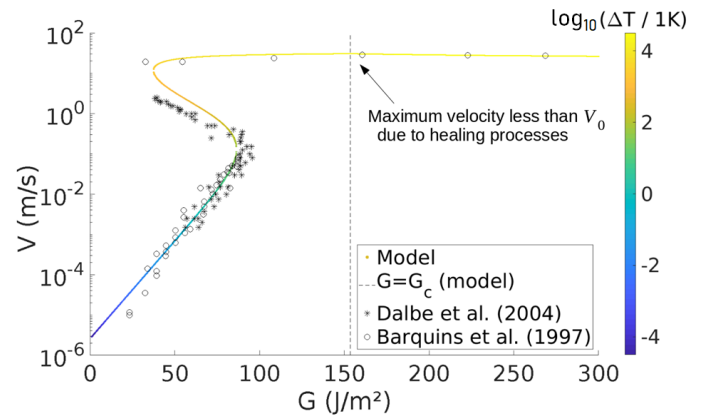


Fig. 11 Fit of the Scotch<sup>®</sup> 3M 600 data<sup>5,6</sup> with a model including healing processes. The unstable (middle) branch of the model should not necessarily match the data point which are averaged  $G$  and  $V$  values for a front that stick-slips.

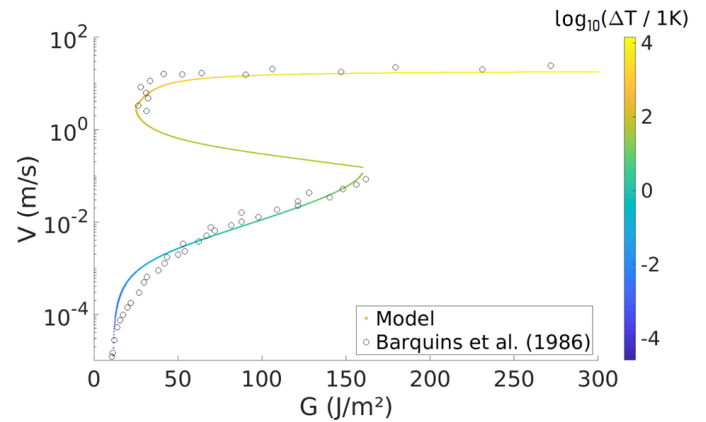


Fig. 12 Fit of the peeling data for another roller tape: Scotch<sup>®</sup> 3M 602 data<sup>7</sup>. The lack of linearity at low velocity calls for healing processes in our model. Note also the curvature on the lower end of the high velocity branch, not present in the other data sets that we show but rather compatible with our proposed model.

not disregarding healing, and compares it with the tape data. The match is there improved compared to the fit presented in Fig. M4 as we have now an additional degree of freedom. The fit parameters in this figure are as follow:  $\xi = 9 \text{ nm}$ ,  $V_0 = 70 \text{ m s}^{-1}$ ,

$G_c = 154 \text{ J m}^{-2}$ ,  $G_h = 200 \text{ J m}^{-2}$ ,  $\phi \sim 1$ ,  $\lambda = 0.2 \text{ J s}^{-1} \text{ m}^{-1} \text{ K}^{-1}$ ,  $C = 10^6 \text{ J m}^{-2} \text{ K}^{-1}$ ,  $l = 1 \text{ nm}$  and  $T_0 = 296 \text{ K}$ .

Note that Barquins *et al.*<sup>7</sup>, who released part of the data presented in Fig. 11, also provided similar measurements for another type of roller tape, Scotch<sup>®</sup> 3M 602 (see Ref.<sup>7</sup>, in French). For this new medium, an asymptote does seem to display at low velocity on the  $(G, V)$  plot, calling for healing processes in our description, as shown in Fig. 12. We there propose a fit with the following parameters:  $\xi = 40 \text{ nm}$ ,  $V_0 = 200 \text{ m s}^{-1}$ ,  $G_c = 500 \text{ J m}^{-2}$ ,  $G_h = 480 \text{ J m}^{-2}$ ,  $\phi = 60\%$ ,  $\lambda = 0.3 \text{ J s}^{-1} \text{ m}^{-1} \text{ K}^{-1}$ ,  $C = 10^6 \text{ J m}^{-3} \text{ K}^{-1}$ ,  $l = 1 \text{ nm}$  and  $T_0 = 296 \text{ K}$ .

## References

- 1 J. Scheibert, C. Guerra, F. Célarié, D. Dalmas and D. Bonamy, *Phys. Rev. Lett.*, 2010, **104**, 045501.
- 2 M. Hattali, J. Barés, L. Ponson and D. Bonamy, *THERMEC* 2011, 2012, pp. 920–924.
- 3 J. Barés, M. L. Hattali, D. Dalmas and D. Bonamy, *Physical Review Letters*, 2014, **113**,.
- 4 T. Vincent-Dospital, R. Toussaint, A. Cochard, K. J. Måløy and E. G. Flekkøy, *Physical Review Materials*, 2020, **4**, 023604.
- 5 M.-J. Dalbe, S. Santucci, P.-P. Cortet and L. Vanel, *Soft Matter*, 2014, **10**, 132–138.
- 6 M. Barquins and M. Ciccotti, *International Journal of Adhesion and Adhesives*, 1997, **17**, 65 – 68.
- 7 M. Barquins, B. Khandani and D. Maugis, *Compte Rendu de l'Académie des Sciences Paris*, 1986, **303**, 1575–1519.